

# Effects of structural anisotropy on deformation and damage of a duplex stainless steel under high strain rate loading

C. Li<sup>a,b</sup>, J.Y. Huang<sup>a</sup>, X.C. Tang<sup>c</sup>, H.W. Chai<sup>a</sup>, X.H. Xiao<sup>d</sup>, Z.D. Feng<sup>a,\*\*</sup>, S.N. Luo<sup>a,b,\*</sup>

<sup>a</sup> The Peac Institute of Multiscale Sciences, Chengdu, Sichuan 610031, PR China

<sup>b</sup> Key Laboratory of Advanced Technologies of Materials, Ministry of Education, Southwest Jiaotong University, Chengdu, Sichuan 610031, PR China

<sup>c</sup> Department of Engineering Mechanics, South China University of Technology, Guangzhou, Guangdong 510640, PR China

<sup>d</sup> Advanced Photon Source, Argonne National Laboratory, Argonne, IL 60439, USA

## ARTICLE INFO

### Keywords:

Duplex stainless steel  
Anisotropy  
Deformation  
Damage evolution  
EBSD

## ABSTRACT

Duplex stainless steel (DSS) with pronounced microstructural anisotropy, is shock-loaded along normal direction, transverse direction and rolling direction to investigate the effects of structural anisotropy on high strain rate deformation and damage. Hugoniot elastic limit (HEL) and spall strength are obtained from free surface velocity histories. The recovered samples are characterized with electron backscatter diffraction and x-ray computed tomography. HEL shows negligible anisotropy and is dominated by the weaker austenite phase. Spall strength shows anisotropy for incipient spallation but not for full spallation. Plastic deformation and damage depend on the mismatch in sound speed and strength between ferrite and austenite. Damage nucleates at phase boundaries, and propagates as cleavage cracks in the textured ferrite; the propagation is blocked by austenite. These factors coupled with different stress states induced by different impact velocities contribute to DSS's anisotropic or isotropic response.

## 1. Introduction

Duplex (austenite-ferrite) stainless steel 2205 (DSS) has excellent anti-corrosion and mechanical properties, and are widely used in, e.g., pressure vessels, chemical tankers, paper machines, and offshore applications [1,2]. To equalize the proportions of the two phases, hot and cold rolling are applied, followed by suitable annealing and quenching [3,4]. Pronounced structural anisotropy is resulted during rolling; anisotropic mechanical responses (deformation and damage) have been observed under normal loading conditions [5]. However, deformation and damage of DSS under high strain rate loading such as planar impact, have rarely been explored.

Anisotropy in mechanical properties of DSS was firstly investigated in static tensile loading. Its yield strength is higher along the transverse direction (TD) compared to the rolling direction (RD) [6–8], due to the texture of ferrite. Impact fracture toughness is higher for loading along TD than the normal direction (ND) because austenite impedes damage coalescence as demonstrated by Charpy impact experiment [9,10].

Nonetheless, the effects of structural anisotropy on Hugoniot elastic limit (HEL, yield stress), and spall strength (dynamic tensile strength) under plate impact are not necessarily the same as in lower strain rate [11–13], uniaxial stress tension experiments, since strain rate effects

and stress conditions (1D strain vs 1D stress) need to be considered. HEL and spall strength of 7010-T6 aluminum alloy [14] are the highest in the longitudinal direction, similar to uniaxial stress experiment. On the other hand, spall strength is anisotropic due to heterogeneous void nucleation, while the anisotropy is weak in HEL for structurally anisotropic 1080 eutectoid steel [15]. HEL and spall strength of Zr, Ta, and HY-100 steel [16] show minor anisotropy, but become strongly anisotropic during quasi-static loading.

For DSS, ferrite as a hard, brittle phase and austenite as a soft, ductile phase, play different roles in deformation and damage process [8,17]. Residual stress measured with X-ray diffraction [18] during loading is lower in RD compared with TD owing to anisotropic plastic deformation in both phases. More plastic deformation occurs in austenite in TD, while plastic deformation in ferrite occurs along the 45° direction in static experiments [7,8]. Cyclic loading experiments on DSS [19,20] show heterogeneously distributed cavities, which propagate as cleavage cracks in ferrite along specific directions, and plastically grow into austenite.

In this work, we investigate systematically the effect of structure anisotropy of DSS on its deformation and damage under gas gun impact, and make connections between macroscopic properties and microstructure features such as ferrite, austenite and phase boundaries.

\* Corresponding author at: The Peac Institute of Multiscale Sciences, Chengdu, Sichuan 610031, PR China.

\*\* Corresponding author.

E-mail addresses: [zdfeng@pims.ac.cn](mailto:zdfeng@pims.ac.cn) (Z.D. Feng), [sluo@pims.ac.cn](mailto:sluo@pims.ac.cn) (S.N. Luo).

Free-surface velocity histories are measured for RD, TD and ND to derive HEL and spall strength. Scanning electron microscope (SEM), electron back-scattering diffraction (EBSD), and X-ray computed tomography (XCT) are used to characterize deformation and damage for different impact velocities. Section 2 addresses materials, impact experiments and microstructure characterizations. Section 3 presents the results of macroscopic mechanical properties as well as deformation and damage microstructure of shock-recovered samples, followed by discussion in Section 4 and conclusions in Section 5.

## 2. Materials, impact experiments, and microstructure characterizations

### 2.1. Materials

The material studied in this work is 2205 duplex stainless steel (DSS) with a nominal chemical composition (wt%) of C: 0.016, Cr: 22.0, Ni: 5.4, Mo: 3.1, N: 0.16, and Fe: balance. It contains a body-centered-cubic (BCC), ferritic  $\alpha$  phase, and face-centered-cubic (FCC), austenitic  $\gamma$  phase. These two phases are related approximately by the Kurdjumov–Sachs crystallographic relationships [17]: one  $\{111\}_\gamma$  parallel to one  $\{110\}_\alpha$  and one  $\langle 111 \rangle_\alpha$  parallel to one  $\langle 110 \rangle_\gamma$  on those close-packed planes.

A pseudo-3D phase map obtained from EBSD analysis (see below) is presented in Fig. 1a. Elongated, flake-like, islands of the austenite phase are dispersed in the ferritic matrix. Their shape and size vary, and their average dimensions are  $\sim 70 \mu\text{m}$ ,  $30 \mu\text{m}$  and  $10 \mu\text{m}$  along RD (rolling direction), TD (transverse direction), and ND (normal direction), respectively. The volume ratio of the ferritic phase to the austenitic phase

is approximately 1. The kernel average misorientation map (Fig. 1b) indicates negligible residual strain after a series of thermal treatment. Each austenite or ferrite patch may consist of several grains, and some austenite grains contain annealing twins after hot rolling. The inverse pole figures in Fig. 1c show relatively strong  $\langle 001 \rangle$  ND texture in the ferrite phase, and  $\langle 001 \rangle$  TD texture in the austenite phase.

The DSS material has a bulk density  $\rho_0$  of  $7.85 \text{ g cm}^{-3}$ . Its longitudinal ( $C_L$ ) and transverse ( $C_T$ ) sound velocities are measured with the ultrasonic method and show pronounced anisotropy.  $C_L$  is  $5818 \text{ ms}^{-1}$ ,  $6067 \text{ ms}^{-1}$  and  $5898 \text{ ms}^{-1}$ , and  $C_T$  is  $3163 \text{ ms}^{-1}$ ,  $3201 \text{ ms}^{-1}$  and  $3335 \text{ ms}^{-1}$ , respectively, along ND, TD and RD. The bulk sound velocity  $C_B$  and Poisson's ratio  $\nu$  are calculated from  $C_L$  and  $C_T$  [21], and their average values are  $C_B = 4810 \text{ ms}^{-1}$ , and  $\nu = 0.29$ .

### 2.2. Plate impact experiments

We perform plate impact experiments using a 14-mm bore diameter single-stage gas gun. The flyer and sample are of a disk shape with a diameter of 13.5 mm and 14 mm, and their thicknesses are 1.5 mm and 3 mm, respectively. The schematic setup of the impact experiments is shown in Fig. 2a. A flyer plate (5) is attached to a polycarbonate sabot (1), with a recess (7) behind it. When the solenoid valve is fired, compressed helium is released from a high-pressure gas reservoir into the gun barrel (3), accelerating the sabot and flyer plate assembly. Upon exiting the muzzle, the flyer plate impacts the target or sample (6) under consideration. The flyer plate velocity is measured with an optical beam block system (4), and the free surface velocity of the target, with a Doppler pin system or DPS (10). Optical signals are analyzed to deduce velocity histories via fast Fourier transformation. The muzzle,

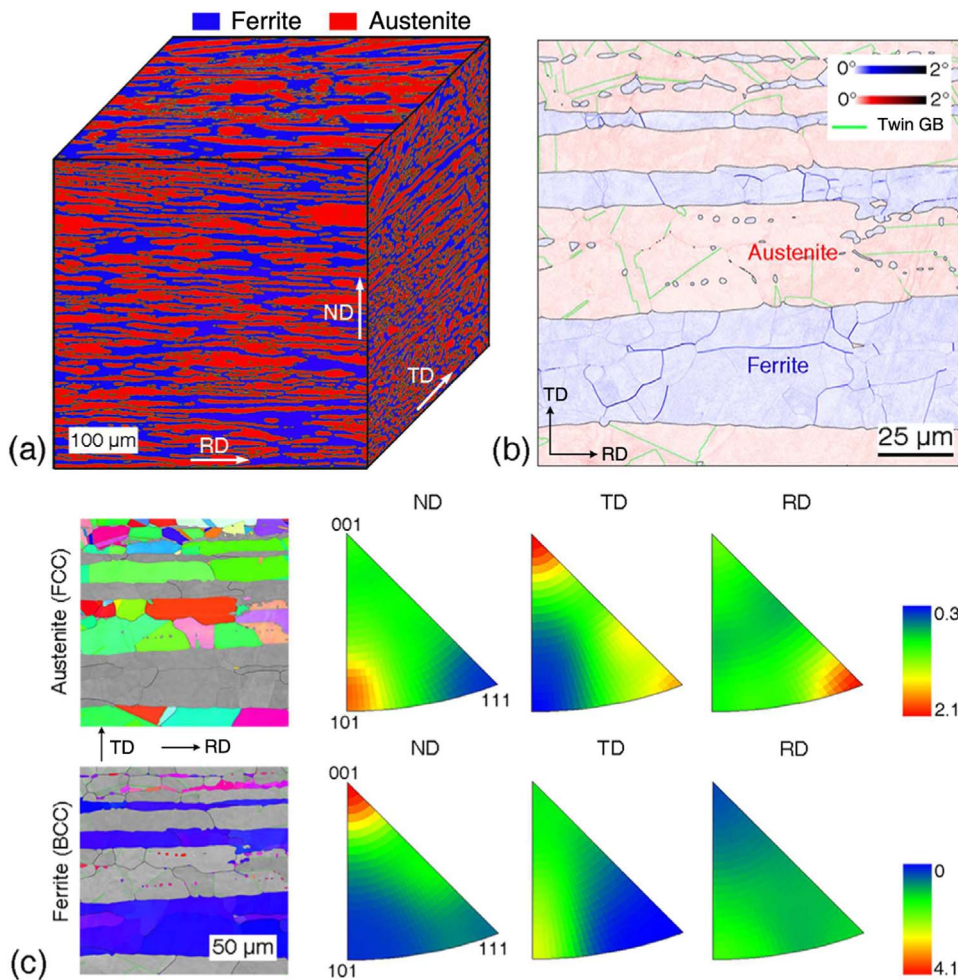
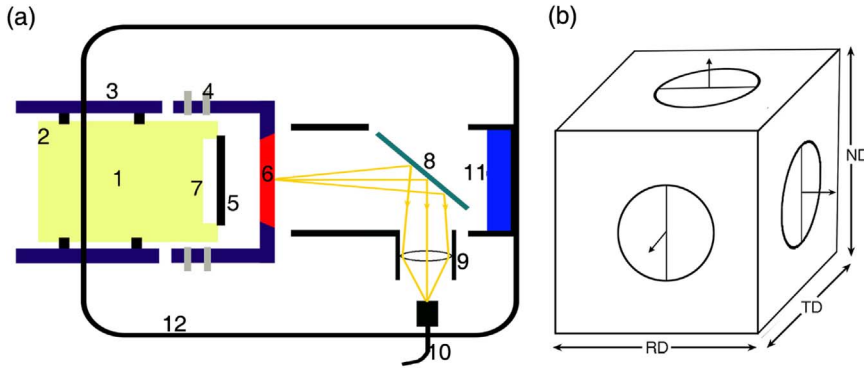


Fig. 1. Microstructural characterization of the as-received DSS. (a) Pseudo-3D phase map. (b) Grain boundaries and phases mapped with kernel average misorientation (KAM). (c) Orientation maps and texture figures of individual phases. RD: rolling direction; TD: transverse direction; ND: normal direction.



**Fig. 2.** (a) Schematic setup for plate-impact experiments. 1: polycarbonate sabot; 2: O-ring; 3: gun barrel; 4: optical fibers and detectors for an optical beam block system; 5: flyer plate; 6: sample; 7: recess for release waves; 8: mirror; 9: lens; 10: optical fiber connected to a Doppler pin system (DPS); 11: soft materials; 12: vacuum chamber. (b) Illustration of loading directions (marked with single-headed arrows) of disk-shaped samples with respect to RD, TD and ND; the lines in the circles represent cutting planes for microstructural characterization.

target and diagnostics are located in a vacuum chamber (12). The shocked samples are soft-recovered [22,23] with soft materials (11) for metallurgical characterizations. The tilt of impact is below 5 mrad as determined from multipoint DPS measurements and the uncertainties in flyer plate and free surface velocity measurements are within 1%.

Plate impact experiments are conducted at low and high impact velocities to induce incipient and full spallation, respectively. To study the effects of structural anisotropy as shown above, the samples are prepared and shock-loaded along RD, TD and ND. Samples with different orientations are harvested. Sample preparation scheme (marked by circles) and loading directions (arrows) are illustrated in Fig. 2b.

### 2.3. Microstructure characterizations

The samples recovered from spallation experiments are characterized with XCT, SEM, EBSD. XCT is performed at the beamline 2-BM at the Advanced Photon Source, and the details were presented elsewhere [24,25]. Recovered samples are sectioned into two halves along specific directions, ground and polished with 1  $\mu\text{m}$  and 0.3  $\mu\text{m}$  alumina particles, and then electro-polished in a 5% perchloric acid and 95% ethanol at 50 V, with a Cu rod and the sample as electrodes. EBSD characterizations are performed using a FEI Quanta 250 FEG-SEM equipped with Oxford EBSD detector and HKL channel 5 OIM software, with a 30 kV voltage, 15 mm working distance, and 70° tilt. Regions of interest for SEM and EBSD are in the central portion which are not affected by edge release.

## 3. Results

### 3.1. Free surface velocity analysis

Nine impact experiments are performed at different impact velocities along three orientations (RD, TD, and ND). Free surface velocity histories,  $u_{fs}(t)$ , are presented in Fig. 3, showing no spallation (dashed lines), incipient spallation (thick lines), and full spallation (thin lines).

We use the velocity profile labeled with A–H to illustrate the process of shock compression, subsequent release, and spallation. Segment AB indicates the elastic precursor, and B denotes the Hugoniot elastic limit (HEL). The plastic wave BC develops into a supported, stable shock CD. The arrival of the release fan from the back surface of the flyer plate leads to a velocity drop (DF), and E denotes the elastic-plastic transition upon release. The interaction of this release fan with that initiated from the target free surface gives rise to release and tension in the sample interior, and spallation is resulted when the tensile stress exceeds the tensile or spall strength at a specific loading condition. The ensuing velocity increase (FG and GH) is induced by the arrival of a compression wave originated from the spall plane within the sample. The re-acceleration beginning at F is a typical spall signature, and the slope of FG is quantified as re-acceleration,  $a_{ra}$ . FG is attributed to independent growth of isolated cracks or voids, and GH, to their coalescence [26,27].

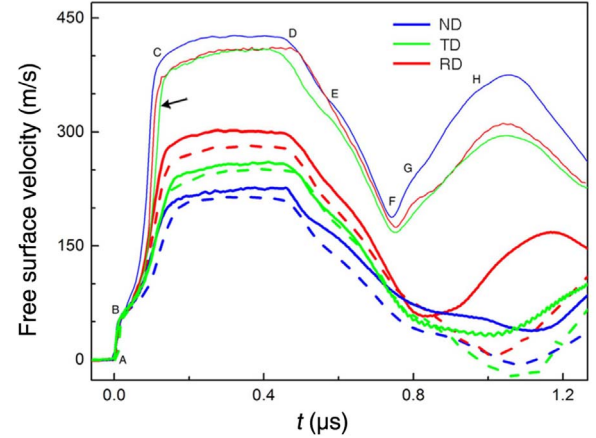


**Fig. 3.** Representative free surface velocity histories. The dashed, thick and thin lines refer to the cases with no spallation, incipient spallation and full spallation, respectively.

Strain rate during elastic compression (e.g., AB in Fig. 3) can be estimated with [28]

$$\dot{\epsilon}_e \approx \frac{1}{2C_L} \left. \frac{du_{fs}(t)}{dt} \right|_{AB}. \quad (1)$$

The stress at HEL is calculated as

$$\sigma_{HEL} = \frac{1}{2} \rho_0 C_L u_{fs} \Big|_B. \quad (2)$$

HEL corresponds to the yield point at the 1D strain state, and is 1.15 GPa for DSS. The von Mises yield stress can be obtained from HEL via

$$\sigma_y = \frac{1 - 2\nu}{1 - \nu} \sigma_{HEL}, \quad (3)$$

and  $\sigma_y = 0.68$  GPa.  $\sigma_{HEL}$  and yield stress are independent of impact velocity and loading orientation (no anisotropy in HEL).  $\sigma_{HEL}$  for DSS is within the range for austenite steel (0.5–1.6 GPa) [29–31], and lower than that for ferrite steel (1.8–2.2 GPa) [15,16,27].

Spall strength is calculated from the pullback velocity with the acoustic method as [11,13]

$$\sigma_{sp} \approx \rho_0 C_L \Delta u \frac{1}{1 + \frac{C_L}{C_B}}, \quad (4)$$

where the pullback velocity  $\Delta u = u_{fs,D} - u_{fs,F}$ . The parameters for incipient and complete spallation are summarized in Table 1, and the three shots without spallation (dashed lines in Fig. 3) are not included.

Table 1 shows strong anisotropy in impact velocity leading to incipient spallation and corresponding spall strength, both increasing in the order of ND, TD and RD. For full spallation,  $\sigma_{sp}$  is higher overall compared to incipient spallation, but its anisotropy is much weaker.



**Table 1**

Summary of experimental parameters.  $u_f$ : flyer plate velocity;  $\sigma_{sp}$ : spall strength;  $a_{ra}$ : reacceleration induced by spall pullback.

Spallation	Orientation	$u_f$ ( $\text{ms}^{-1}$ )	$\sigma_{sp}$ (GPa)	$a_{ra}$ ( $10^6 \text{ ms}^{-2}$ )
Incipient	ND	238	3.3	—
	TD	278	4.4	—
	RD	325	5.0	—
Full	ND	455	4.9	1.1
	TD	443	5.0	0.5
	RD	435	4.9	0.8

Another feature in the free surface velocity histories (Fig. 3) is that the time difference between the elastic and plastic wave decreases in the order of ND, RD and TD. A probable reason is that the elastic wave speed increases sequentially while the plastic wave speed remains approximately the same.

### 3.2. Microstructures related to deformation and damage

#### 3.2.1. Shock compression

Microstructure characterization of deformation induced by shock compression is presented in Fig. 4, of an area near the impact surface of recovered samples in the full spallation experiments. The impact surface area experiences full compression but minimum tension. The minor misorientation indicates that plastic deformation is small and mainly accommodated by dislocation slip in both ferrite and austenite phases. Plastic deformation concentrates around phase boundaries, because of the mismatch of ferrite and austenite properties.

We calculate the average misorientation  $\bar{M}$  from kernel misorientation maps (Fig. 1b and Fig. 4a–c) via

$$\bar{M} = \exp \left\{ \frac{1}{N} \sum_{i=1}^N \ln[M(p_i)] \right\}, \quad (5)$$

where  $M(p_i)$  is the misorientation at the  $i$ th pixel on the map [32], and the results are presented in Table 2. The equivalent plastic strain is proportional to  $\Delta\bar{M}$ , the difference in  $\bar{M}$  before and after loading [33].  $\Delta\bar{M}$  is much higher along TD than along ND and RD.  $\Delta\bar{M}$  for austenite is slightly higher for ferrite, indicating higher plastic deformation in austenite.

#### 3.2.2. Incipient spallation

XCT characterizations of the recovered samples with incipient spallation are presented in Fig. 5 for three different loading directions. Microdamage nucleates as voids in all cases. However, these voids grow into cracks with different 3D morphologies during subsequent loading. Sheet-like cracks along the spall plane (Fig. 5a) are observed for the ND-

**Table 2**

Average misorientation  $\bar{M}$  in the ferrite and austenite phases.  $\Delta$  refers to the difference in  $\bar{M}$  before and after loading.

Phase	$\bar{M}/\Delta\bar{M}$ ( $^\circ$ )	As-received	ND	TD	RD
Ferrite	$\bar{M}$	0.166	0.324	0.377	0.303
	$\Delta\bar{M}$	—	0.158	0.211	0.137
Austenite	$\bar{M}$	0.154	0.313	0.401	0.302
	$\Delta\bar{M}$	—	0.159	0.247	0.148

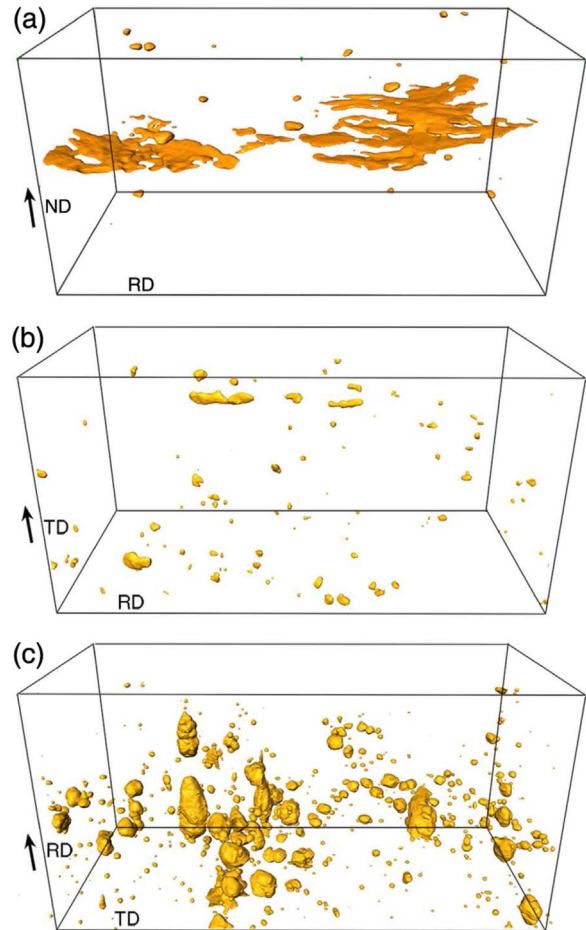


Fig. 5. XCT characterizations of cracks and voids for the incipient spallation cases. (a) ND. (b) TD. (c) RD. The arrows denote shock directions. The sampling volume is  $350 \times 350 \times 700 \mu\text{m}^3$ .

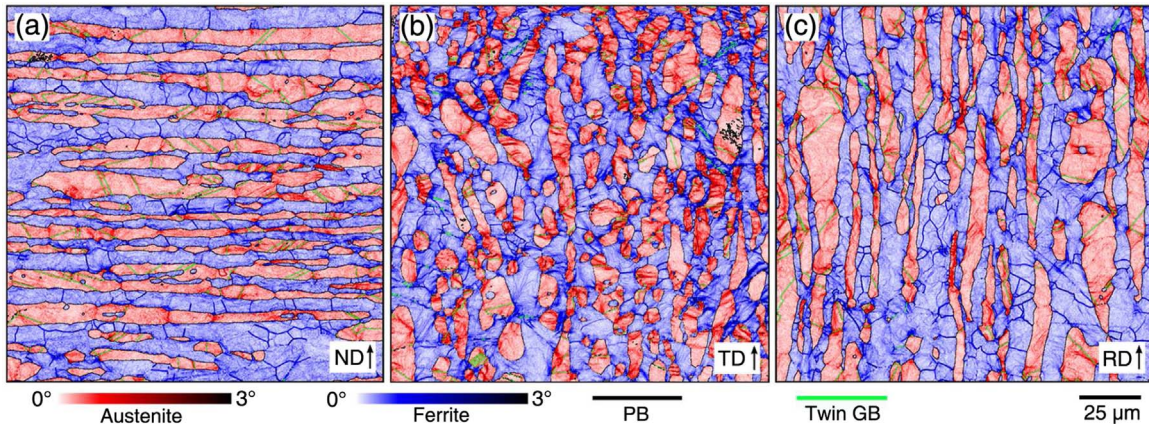


Fig. 4. Typical kernel average misorientation maps near the impact surface in completely spalled samples. (a) ND. (b) TD. (c) RD.

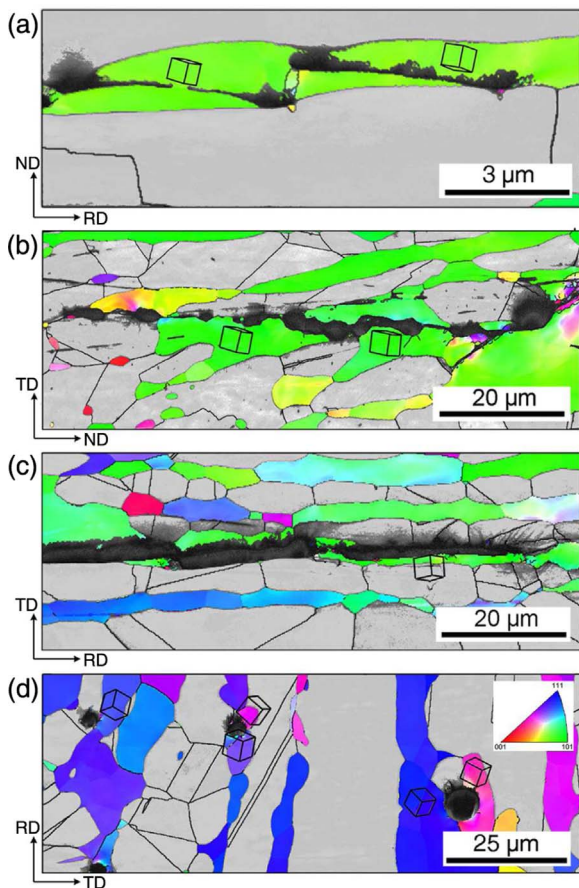


Fig. 6. The inverse pole figure maps of the ferrite phase for the incipient spallation cases. (a) ND. (b, c) TD. (d) RD. The cubes mark local crystal orientations.

loading, while needle-like cracks and spherical or ellipsoidal cracks form for the TD- (Fig. 5b) and RD-loading (Fig. 5c), respectively.

The different fracture morphologies are attributed to structural anisotropy in DSS and loading orientations. Voids initiate at phase boundaries (Fig. 6a and d), which serve as the weak zones. Voids grow and coalesce into microcracks, which propagate along phase boundaries (Fig. 6c) [9] or across the ferrite phase due to cleavage fracture along  $\{100\}$  crystallographic planes [34]. Cracks tend to grow and propagate perpendicular to the shock direction (the largest tensile stress component) during spallation. As a result, cleavage cracking in the ferrite grains is easier for ND and TD than RD, since the  $\{100\}$  planes in the ND and TD samples are aligned parallel to the spall plane.

However, cracks are likely to be blocked by the austenite phase (Fig. 5d), which is softer but more ductile than the ferrite phase. The austenite phase is flat and cuts the ferrite matrix into numerous “sheets” perpendicular to ND (Fig. 1a). For ND-loading, cleavage fracture occurs with relative ease, and microcracks grow with less hinderance along TD and RD, thus developing into sheet-like cracks. For TD-loading, crack propagation is impeded in ND but is relatively free along RD (Fig. 5f), leading to needle-like cracks. For RD-loading, crack propagation is blocked along TD and ND, and thus only spherical voids form and largely remain isolated [35].

### 3.2.3. Full spallation

EBSD and SEM micrographs of samples with full spallation are presented in Fig. 7 for ND-, TD- and RD-loading. Damage degree of the ND sample ( $\sim 30\%$ ) is much higher than that of TD and RD samples ( $\sim 11\%$ ). The ND sample (Fig. 7a) shows a large, coalesced, principal crack, different from the scattered, winding, cracks in the TD and RD samples. One probable reason is the rapid damage growth and

coalescence along phase boundaries which are parallel to the spall plane in the ND sample (Fig. 7d). This is also consistent with the steepest slope of *FG* (spall-induced reacceleration) in the free surface velocity history (Fig. 3b).

Damage nucleates as microvoids (the dashed circles in Fig. 7d–f) mainly at phase and grain boundaries. Some voids grow into bigger ones (the arrows in Fig. 7d–f) and coalesce into facets, forming small dimples in Fig. 7j–l. Others grow into cracks along the TD–RD rolling plane in three loading geometries (Fig. 7d–f), and play different roles in ensuing coalescence. For loading along ND, cracks are all parallel to the spall plane. The staggered principal cracks or facets (red arrows in Fig. 7j) can only be connected via shear plastic deformation and cracking (white arrows in Fig. 7g), and develop into a relatively flat fracture surface. This is consistent with the ridges (red dash arcs in Fig. 7j) on the fracture surface. The coalescence mode for loading along TD is similar to that along ND. For loading along RD, cracks are mostly perpendicular to the spall plane (Fig. 7f). They serve as a bridge (Fig. 7i) connecting the staggered facets, leading to a rugged fracture surface (Fig. 7l). These different coalescence modes are also reflected in the free surface velocity histories: the transition point *G* for RD is much more obvious than those for ND and TD (Fig. 3).

Since damage and 2D fracture morphologies are similar for loading along RD and TD, postmortem XCT is performed to resolve the differences in their damage and fracture characteristics. Small spherical voids and long cracks are elongated along the TD–RD plane, in both TD and RD samples (Fig. 8a–b). In the TD sample, damage concentrates near the spall plane. The RD sample outruns the TD sample in both void/crack number and size, but voids are distributed more evenly lengthwise. Those damage sites form “sheets” along the loading direction. At the same impact velocity, damage nucleation and coalescence for the TD loading are more difficult compared to the RD loading, consistent with the less steep slope of *FG* (Fig. 3).

## 4. Discussion

HEL of a pure austenite steel is generally lower than that of its ferrite counterpart [15,16,27,29–31]. As seen from the EBSD analysis, plastic deformation is indeed more pronounced in the austenite phase of recovered DSS samples. Upon shock, the softer austenite phase yields before the ferrite phase and induces perturbations propagating toward the free surface. Consistently, HEL of DSS obtained from free surface velocity histories is similar to that of pure austenite, but lower than that of pure ferrite. Austenite has a FCC structure with high crystal symmetry, weak texture and relatively frequent incidence of pyramidal slip during high-strain-rate loading [16]. These factors contribute to the weak anisotropy in HEL of DSS given its microstructural anisotropy. However, HEL was found to be dependent on grain shape with a DSS [36]. Further work on microstructure effects is certainly desired.

It is also interesting to explore strain rate effects on yield and damage. As a complement to high strain rate loading, we also conduct low and medium strain rate compression experiments with a materials testing system (MTS) and split Hopkinson pressure bar (SHPB), respectively (Fig. 9a). For the low and medium strain rate tensile experiments, the yield stress is anisotropic and dominated by the textured ferrite [6,9] (higher than that of pure austenite steel), while gas gun loading displays negligible anisotropy in the yield stress (Fig. 9b). In addition, the yield stress for the medium strain rate loading ( $2.5 \times 10^3 \text{ s}^{-1}$ ) is much higher than that of the planar impact (gas gun: GG) with higher strain rate (estimated by Eq. (1),  $4.5 \times 10^5 \text{ s}^{-1}$ ), since the yield stress is dominated by harder ferrite and softer austenite, respectively.

The non-volumetric shear strain is induced for loading along phase boundary both in shock compression and subsequent spallation [37]. The amplitude of shear strain is positively correlated with the number of phase boundaries parallel to the shock direction (decreasing in the order of RD, TD and ND, Fig. 1a), and the degree of mismatch in sound



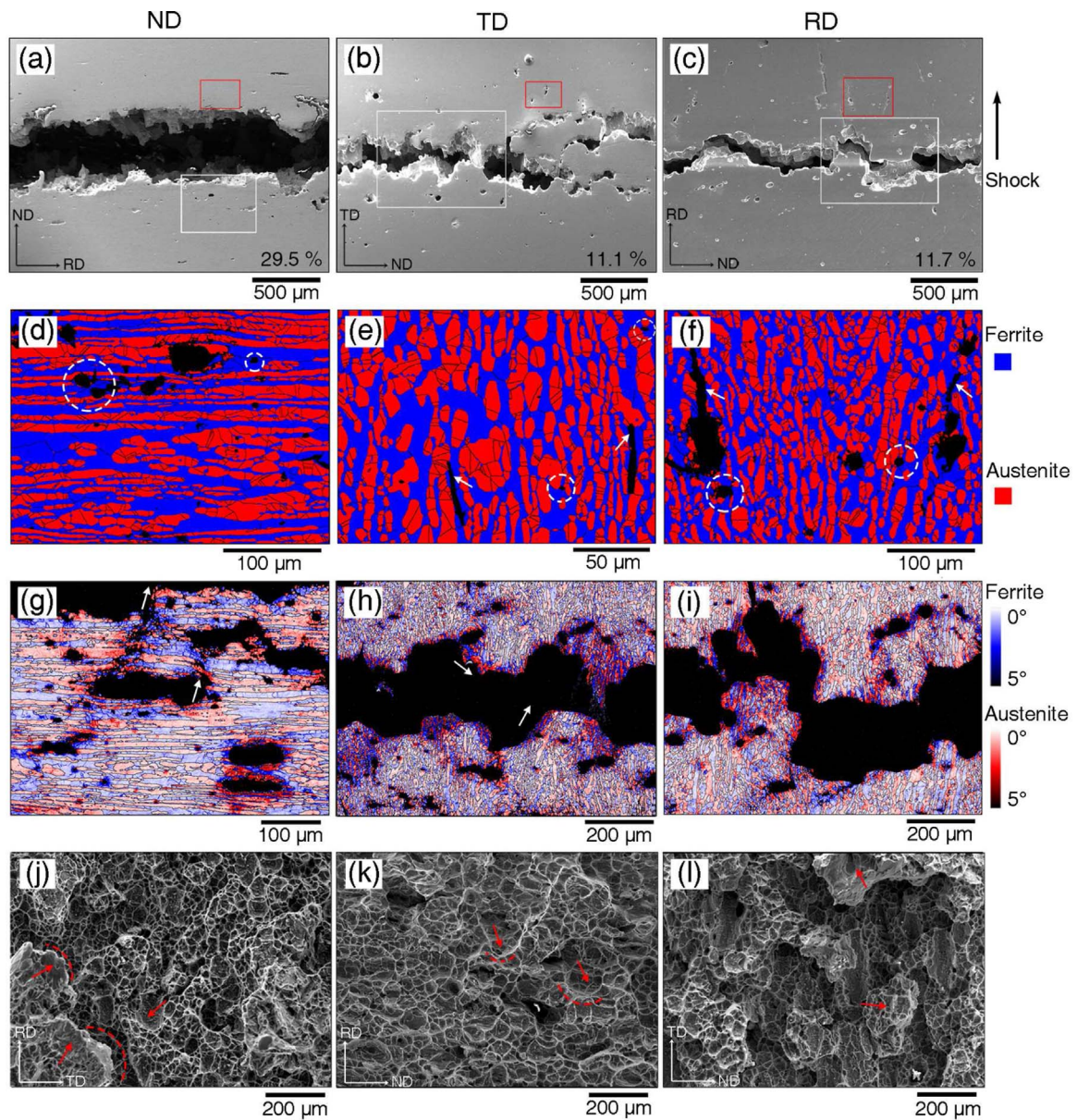


**Fig. 7.** SEM and EBSD micrographs for the full spallation cases for loading along ND, TD and RD. (a)–(c) SEM micrographs. The areas delimited by the red and white rectangles are chosen for EBSD analysis. The areal percentage of damage is noted at the bottom right corner. (d)–(f) Phase color maps corresponding to the areas indicated by the red rectangles. (g)–(i) Kernel average misorientation maps of the areas indicated by the white rectangles. (j)–(l) SEM fractography.

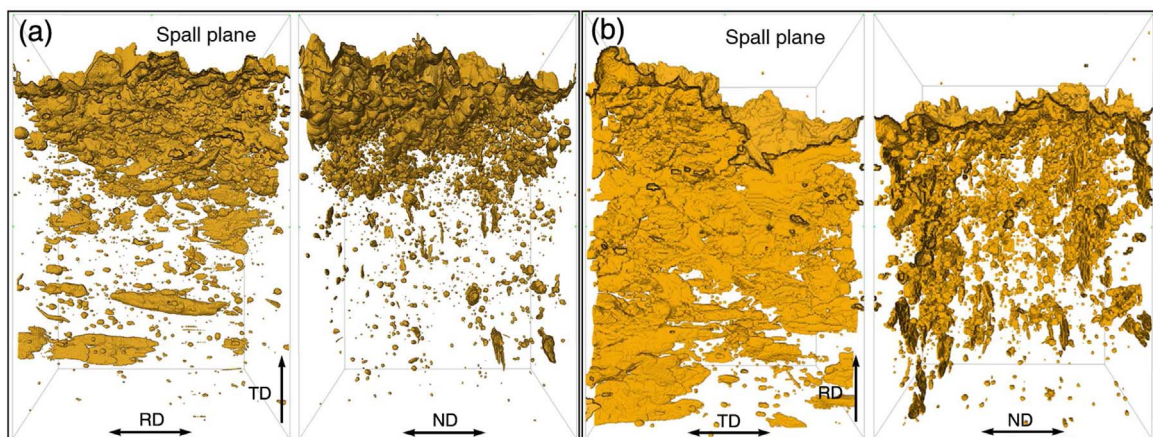


**Fig. 8.** XCT characterizations of spall regions for full spallation cases, TD (a) and RD (b). The sampling volume is 750 × 750 × 1150 μm³.

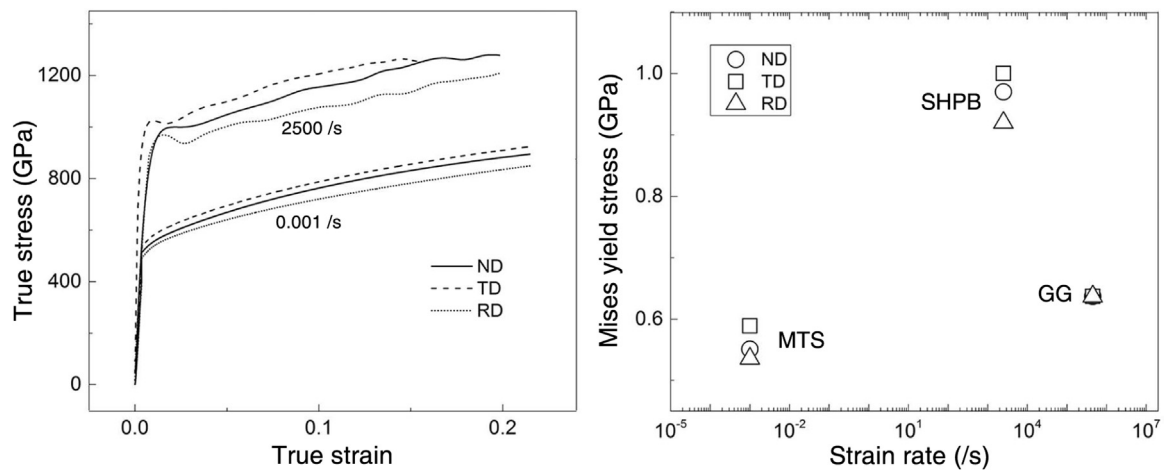


Fig. 9. (a) Representative compressive true stress-strain curves for different loading directions (ND, TD, and RD) at low and medium strain rates. (b) Von Mises yield stress as a function of strain rate. MTS: materials testing system; SHPB: split Hopkinson pressure bar; GG: gas gun.

velocity and yield stress between the ferrite and austenite phases [38]. Ferrite has higher elastic modulus and yield strength than austenite, and the excess decreases in the order of TD, ND and RD during cyclic loading [39]. Therefore, the sound speed of ferrite with lower density [38,40] is higher than that of austenite, and the difference between them decreases in the order of TD, ND and RD.

Shear strain promotes plastic deformation, while dilatational strain leads to void/crack opening in spallation [37]. Plastic deformation is more pronounced for loading along TD than along ND and RD. Shear is coupled with tension and may curtail void nucleation and growth via plastic flow [37]. Thus, it is more difficult for damage nucleation and evolution for loading along TD.

For incipient spall, cleavage only occurs in ferrite grains on {100} planes approximately parallel to the spall plane. The things that {001} directions of the ferrite most preferentially orient in ND, then TD, then RD (Fig. 1c) determine the possibility of cleavage, which decreases in the order of ND, TD, and RD loading. The cleavage cracks are blocked by the austenite phase during propagation. The extension length is determined by the distance between neighboring austenite islands in the ferrite matrix along the spall plane, which increases in the order of ND, TD and RD (Fig. 1a). Therefore, the probability and propagation distance of cleavage fracture are both the highest for the ND loading and the lowest for the RD loading, corresponding the lowest and highest spall strength, respectively.

Higher impact velocities for full spallation leads to a more hydrostatic stress state, resulting in similar spall strengths for loading along ND, TD and RD. Damage nucleates and grow initially as voids, and tends to propagate along the weakest plane, i.e., the TD-RD rolling plane. Those cracks are perpendicular to the spall plane and abounding in the RD sample, acting as the bridge to connect facets to form completely fractured surface. On the other hand, the facets only coalesce by shear cracks because the cracks are parallel to the spall plane (ND) or small in quantity (TD).

Therefore, spall strength is dictated by the initial stage of damage nucleation and growth [41,42]. Low-energy brittle cracks corresponds to low spall strength, while high-energy ductile voids, to higher spall strength. The anisotropy or isotropy in spall strength is due to anisotropic or isotropic damage evolution, respectively. The anisotropic initial damage evolution is controlled by the anisotropy in microstructure and stress state. For the former, damage tends to propagate along the directional features, such as cleavage plane, glide plane, grain boundary and phase boundary. For the latter, damage can only evolve along the spall plane (following the maximum tensile stress) in current incipient spallation cases such as previous 1080 eutectoid steel [15], incipient spallation of this work. While for complete spallation, quasi-

hydrostatic-stress state is achieved, so damage nucleates as voids regardless of the structure anisotropy, and the anisotropy in spall strength is reduced considerably.

## 5. Conclusions

Free-surface velocity history measurements, and SEM, EBSD, and XCT characterizations are performed on structurally anisotropic DSS subjected to impact loading. Our main conclusions are

- HEL shows weak anisotropy, and its value is similar to pure austenite. The weak-textured, softer, austenite phase dominates HEL, as opposed to the harder ferrite which dictates the yield stress at low and medium strain rates.
- Loading along TD leads to more pronounced deformation but lesser damage. The largest mismatch in sound velocity and yield strength between ferrite and austenite gives rise to largest shear deformation for the TD loading. Shear interacts with tension and may curtail void nucleation and growth via plastic flow.
- For incipient spallation, microvoids nucleate at phase boundaries, and grow into sheet-like, needle-like, and spherical shapes for ND, TD, and RD loading, respectively. Cleavage fracture occurs in strong-textured ferrite and blocked by austenite; its probability of occurrence and propagation distance are the highest for ND loading and lowest for RD loading.
- For full spallation, macrovoids likely nucleate at phase boundaries and grow along the weakest plane (the TD–RD rolling plane), and coalesce by the damage connection (RD) or shear cracks (ND and TD). Cracks in the RD sample outrun those in the ND and TD samples in size or number.
- Anisotropy in spall strength is pronounced for incipient spallation but negligible for full spallation, because the stress state is more anisotropic in the former case.

## Acknowledgments

This work was partially supported by the National Key R&D Program of China (Grant No. 2017YFB0702002) and NSFC (Grant Nos. 11627901, 11372113, and 11672110). Use of the Advanced Photon Source, an Office of Science User Facility operated for the US Department of Energy (DOE) Office of Science by Argonne National Laboratory, was supported by the US DOE under contract No. DE-AC02-06CH11357.



## References

- [1] R.N. Gunn, Duplex Stainless Steels: Microstructure, Properties and Applications, Woodhead Publishing, 1997.
- [2] I. Alvarez-Armas, S. Degallaix-Moreuil, Duplex Stainless Steels, John Wiley, 2013.
- [3] D.S. Bergstrom, J.J. Dunn, J.F. Grubb, W.A. Pratt, Duplex stainless steels, US Patent 6,623,569 (Sep. 23 2003).
- [4] R. Dakhlaoui, C. Braham, A. Baczmanski, Mechanical properties of phases in austenite-ferritic duplex stainless steel-surface stresses studied by X-ray diffraction, Mater. Sci. Eng. A 444 (1) (2007) 6–17.
- [5] M. Igarashi, K. Kondo, K. Ogawa, M. Ueda, T. Mori, Duplex stainless steel, US Patent 5,849,111 (Dec. 15 1998).
- [6] W. Hutchinson, K. Ushioda, G. Runnsjö, Anisotropy of tensile behaviour in a duplex stainless steel sheet, Mater. Sci. Tech. 1 (9) (1985) 728–736.
- [7] J.J. Moverare, M. Odén, Influence of elastic and plastic anisotropy on the flow behavior in a duplex stainless steel, Metall. Mater. Trans. A 33 (1) (2002) 57–71.
- [8] J. Song, P. Bate, Plastic anisotropy in a superplastic duplex stainless steel, Acta Mater. 45 (7) (1997) 2747–2757.
- [9] R. Lula, Duplex Stainless Steels, ASM, Metals Park, OH, 1983.
- [10] L. Devillers-Guerville, J. Besson, A. Pineau, Notch fracture toughness of a cast duplex stainless steel: modelling of experimental scatter and size effect, Nucl. Eng. Des. 168 (1) (1997) 211–225.
- [11] G.I. Kanel, Spall fracture: methodological aspects, mechanisms and governing factors, Int. J. Fract. 163 (1–2) (2010) 173–191.
- [12] S. Fensin, D. Jones, E. Walker, A. Farrow, S. Imhoff, K. Clarke, C. Trujillo, D. Martinez, G. Gray III, E. Cerreta, The effect of distribution of second phase on dynamic damage, J. Appl. Phys. 120 (8) (2016) 085901.
- [13] T. Antoun, Spall Fracture, Springer Science, 2003.
- [14] R. Vignjevic, N. Bourne, J. Millett, T. De Vuyst, Effects of orientation on the strength of the aluminum alloy 7010-T6 during shock loading: experiment and simulation, J. Appl. Phys. 92 (8) (2002) 4342–4348.
- [15] G.T. Gray III, N. Bourne, J. Millett, M. Lopez, K.S. Vecchio, M.D. Furnish, N.N. Thadhani, Y. Horie, Influence of microstructural anisotropy on the spallation of 1080 eutectoid steel, in: AIP Conference Proceedings, vol. 620, AIP, 2002, pp. 479–482.
- [16] G. Gray III, N. Bourne, K. Vecchio, J. Millett, Influence of anisotropy (crystallographic and microstructural) on spallation in Zr, Ta, HY-100 steel, and 1080 eutectoid steel, Inter. J. Fract. 163 (1–2) (2010) 243–258.
- [17] H.D. Solomon, T. Devine Jr, Duplex stainless steels—a tale of two phases, in: Duplex stainless steels, 1982, pp. 693–756.
- [18] J. Johansson, M. Odén, X.-H. Zeng, Evolution of the residual stress state in a duplex stainless steel during loading, Acta Mater. 47 (9) (1999) 2669–2684.
- [19] J. Besson, L. Devillers-Guerville, A. Pineau, Modeling of scatter and size effect in ductile fracture: application to thermal embrittlement of duplex stainless steels, Eng. Fract. Mech. 67 (2) (2000) 169–190.
- [20] S. Bugat, J. Besson, A.-F. Gourgues, F. N'Guyen, A. Pineau, Microstructure and damage initiation in duplex stainless steels, Mater. Sci. Eng. A 317 (1) (2001) 32–36.
- [21] H. Ledbetter, Sound velocities and elastic constants of steels 304, 310, and 316, Met. Sci. 14 (12) (1980) 595–596.
- [22] R.W. Minich, J.U. Cazamias, M. Kumar, A.J. Schwartz, Effect of microstructural length scales on spall behavior of copper, Metall. Mater. Trans. A 35 (9) (2004) 2663–2673.
- [23] M. Chen, J. McCauley, D. Dandekar, N. Bourne, Dynamic plasticity and failure of high-purity alumina under shock loading, Nat. Mater. 5 (8) (2006) 614–618.
- [24] T. Li, D. Fan, L. Lu, J. Huang, F. Zhao, M. Qi, T. Sun, K. Fezzaa, X. Xiao, X. Zhou, et al., Dynamic fracture of C/SiC composites under high strain-rate loading: microstructures and mechanisms, Carbon 91 (2015) 468–478.
- [25] E. Padilla, V. Jakkali, L. Jiang, N. Chawla, Quantifying the effect of porosity on the evolution of deformation and damage in Sn-based solder joints by X-ray microtomography and microstructure-based finite element modeling, Acta Mater. 60 (9) (2012) 4017–4026.
- [26] A. Zurek, W. Thissell, J. Johnson, D. Tonks, R. Hixson, Micromechanics of spall and damage in tantalum, J. Mater. Process. Tech. 60 (1) (1996) 261–267.
- [27] C. Li, B. Li, J. Huang, H. Ma, M. Zhu, J. Zhu, S. Luo, Spall damage of a mild carbon steel: effects of peak stress, strain rate and pulse duration, Mater. Sci. Eng. A 660 (2016) 139–147.
- [28] M.A. Meyers, K.K. Chawla, Mechanical behavior of materials, 2 Cambridge university press, Cambridge, 2009.
- [29] M. Werdiger, B. Glam, L. Bakshi, E. Moshe, Y. Horovitz, S.L. Pistinner, M.L. Elert, W. T. Buttler, J.P. Borg, J.L. Jordan, et al., On the dynamic strength of 304L stainless steel under impact, in: AIP conference proceedings, vol. 142, AIP, 2012, pp. 1149–1152.
- [30] B.H. Sencer, S.A. Maloy, G.T. Gray, The influence of shock-pulse shape on the structure/property behavior of copper and 316 L austenitic stainless steel, Acta Mater. 53 (11) (2005) 3293–3303.
- [31] G. Whiteman, P. Keightley, J. Millett, The behaviour of 2169 steel under uniaxial stress and uniaxial strain loading, J. Dyn. Behav. Mater. 2 (3) (2016) 337–346.
- [32] M. Kamaya, Assessment of local deformation using ebsd: quantification of accuracy of measurement and definition of local gradient, Ultramicroscopy 111 (8) (2011) 1189–1199.
- [33] M. Kamaya, Measurement of local plastic strain distribution of stainless steel by electron backscatter diffraction, Mater. Charact. 60 (2) (2009) 125–132.
- [34] J. Nohava, P. Haušild, M. Karlik, P. Bompard, Electron backscattering diffraction analysis of secondary cleavage cracks in a reactor pressure vessel steel, Mater. Charact. 49 (3) (2002) 211–217.
- [35] A. Brown, Q. Pham, E. Fortin, P. Peralta, B. Patterson, J. Escobedo, E. Cerreta, S. Luo, D. Dennis-Koller, D. Byler, et al., Correlations among void shape distributions, dynamic damage mode, and loading kinetics, JOM (2016) 1–9.
- [36] R. Silverstein, D. Eliezer, Influences of hydrogen and textural anisotropy on the microstructure and mechanical properties of duplex stainless steel at high strain rate, J. Mater. Sci. 51 (23) (2016) 10442–10451.
- [37] S. Fensin, J. Escobedo-Diaz, C. Brandl, E. Cerreta, G. Gray, T. Germann, S. Valone, Effect of loading direction on grain boundary failure under shock loading, Acta Mater. 64 (2014) 113–122.
- [38] E. Wielewski, G. Appleby-Thomas, P. Hazell, A. Hameed, An experimental investigation into the micro-mechanics of spall initiation and propagation in Ti-6Al-4 V during shock loading, Mater. Sci. Eng. A 578 (2013) 331–339.
- [39] J. Johansson, M. Odén, Load sharing between austenite and ferrite in a duplex stainless steel during cyclic loading, Metall. Mater. Trans. A 31 (6) (2000) 1557–1570.
- [40] A. Mateo, L. Llanes, N. Akdut, J. Stolarz, M. Anglada, Anisotropy effects on the fatigue behaviour of rolled duplex stainless steels, Int. J. Fatigue 25 (6) (2003) 481–488.
- [41] E.M. Bringa, S. Traiviratana, M.A. Meyers, Void initiation in fcc metals: effect of loading orientation and nanocrystalline effects, Acta Mater. 58 (13) (2010) 4458–4477.
- [42] V. Lubarda, M. Schneider, D. Kalantar, B. Remington, M. Meyers, Void growth by dislocation emission, Acta Mater. 52 (6) (2004) 1397–1408.